Polarization lidar: An extended three-signal calibration approach

Cristofer Jimenez[1], Albert Ansmann[1], Ronny Engelmann[1], Moritz Haarig[1], Jörg Schmidt[2], and Ulla Wandinger[1]

[1]Leibniz Institute for Tropospheric Research, Leipzig, D-04318, Germany
[2]University of Leipzig, Institute for Meteorology, Leipzig, D-04103, Germany

Correspondence to: Cristofer Jimenez (cristofer.jimenez@tropos.de)

Abstract. We present a new formalism to calibrate a three-signal polarization lidar and to measure highly accurate height profiles of the volume linear depolarization ratios under realistic experimental conditions. The methodology considers elliptically polarized laser light, angular misalignment of the receiver unit with respect to the main polarization plane of the laser pulses, and crosstalk between the receiver channels. A case study of a liquid-water cloud observation demonstrates the potential of the new technique. Long-term observations of the calibration parameters corroborate the robustness of the method and the long-term stability of the three-signal polarization lidar. A comparison with a second polarization lidar shows excellent agreement regarding the derived volume linear polarization ratios in different scenarios: a biomass burning smoke event throughout the troposphere and the lower stratosphere up to 16 km height, a dust case and also a cirrus cloud case.

1 Introduction

Atmospheric aerosol particles influence the evolution of clouds and the formation of precipitation in complex and not well understood ways. Strong efforts are needed to improve our knowledge about aerosol-cloud interaction and the parameterization of cloud processes in atmospheric (weather and climate) models, weather forecasts, and especially to decrease the large uncertainties in future climate predictions (IPCC 2013). Besides more measurements in contrasting environments with different climatic and air pollution conditions, new experimental (profiling) methods need to be developed to allow an improved and more direct observation of the impact of different aerosol types and mixtures on the evolution of liquid-water, mixed-phase, and ice clouds occurring in the height range from the upper planetary boundary layer to the tropopause. Active remote sensing is a powerful technique to continuously and coherently monitor the evolution and life cycle of clouds in their natural environment.

Recently, Schmidt et al. (2013, 2014, 2015) introduced the so-called dual-field-of-view (dual-FOV) Raman lidar technique which allows us to measure aerosol particle extinction coefficients (used as aerosol proxy) close to cloud base of a liquid-water cloud layer and to retrieve, at the same time, cloud microphysical properties such as cloud droplet effective radius and cloud droplet number concentration (CDNC) in the lower part of the cloud layer. In this way, the most direct impact of aerosol particles on cloud microphysical properties could be determined. However, the method is only applicable after sun set (during nighttime) and signal averaging of the order of 10-30 minutes is required to reduce the impact of signal noise on the observations to a tolerable level. As a consequence, cloud properties cannot be resolved on scales of 100-200 m horizontal

resolution or 10-30 s. To improve the dual-FOV measurement concept towards daytime observations and shorter signal averaging times (towards time scales allowing us to resolve individual, single updrafts and downdrafts) we developed the so-called dual-FOV polarization lidar method (Jimenez et al., 2017, 2018a). This technique makes use of strong depolarization of transmitted linearly polarized laser pulses in water clouds by multiple scattering of laser photons by water droplets (with typical number concentrations of 100 cm^{-3}). This novel polarization lidar method can be applied to daytime observations with resolutions of 10-30 s. An extended description of the method is in preparation (Jimenez et al., 2018b).

Highly accurate observations of the volume linear depolarization ratio are of fundamental importance for a successful retrieval of cloud microphysical properties by means of the new polarization lidar technique. In this article (part 1 of a series of several papers on the dual-FOV polarization lidar technique), we present and discuss our new polarization lidar setup and how the lidar channels are calibrated. The basic product of a polarization lidar is the volume linear depolarization ratio, defined as the ratio of the cross-polarized to the co-polarized atmospheric backscatter intensity, and is derived from lidar observations of the cross and co-polarized signal components, or alternatively, from the observation of the cross-polarized and total (cross + co-polarized) signal components. Cross and co-polarized denote the plane of linear polarization, orthogonal and parallel to the linear polarization plane of the transmitted laser light, respectively. Reichardt et al. (2003) proposed a robust concept to obtain high-quality depolarization ratio profiles by measuring simultaneously three signal components, namely the cross and co-polarized signal components and additionally the total elastic backscatter signal. We will follow this idea as described in Sect. 2. Reichardt et al. (2003) assumed that the laser pulses are totally linearly polarized. Recent studies, however, have shown that the transmitted laser pulses can be slightly elliptically polarized (David et al., 2012; Freudenthaler, 2016; Bravo-Aranda et al., 2016; Belegante et al., 2018). We will consider this effect in our extended approach of the three-channel depolarization technique. We further extend the formalism by considering realistic strengths of crosstalk between the three channels and we propose a practical inversion scheme based on the determination of the instrumental constants for the retrieval of high temporal resolution volume depolarization ratio profiles.

The article is organized as follows. In Sect. 2, the lidar instrument is described. The new methodology to calibrate the lidar system and to obtain high quality depolarization ratio observations is outlined in Sect. 3. Sect. 4 presents and discusses atmospheric measurements performed to check and test the applicability of the new methodology. Concluding remarks are given in Sect. 5.

2 Lidar setup

A sketch of the instrumental setup, providing an overview of the entire lidar system, is shown in Fig. 1. MARTHA (Multiwavelength Tropospheric Raman lidar for Temperature, Humidity, and Aerosol profiling) has a powerful laser transmitting in total 1~J per pulse at a repetition rate of 30~Hz and has an 80~cm telescope, and is thus well designed for tropospheric and stratospheric aerosol observations (Mattis et al., 2004, 2008, 2010; Schmidt et al., 2013, 2014, 2015; Jimenez

et al., 2017, 2018). MARTHA belongs to the European Aerosol Research Lidar Network (EARLINET) (Pappalardo et al., 2014). We implemented a new three-signal polarization lidar receiver unit to the left side of the large telescope (see Fig. 1). The new receiver setup is composed of three independent telescopes co-aligned with the lidar transmitter.
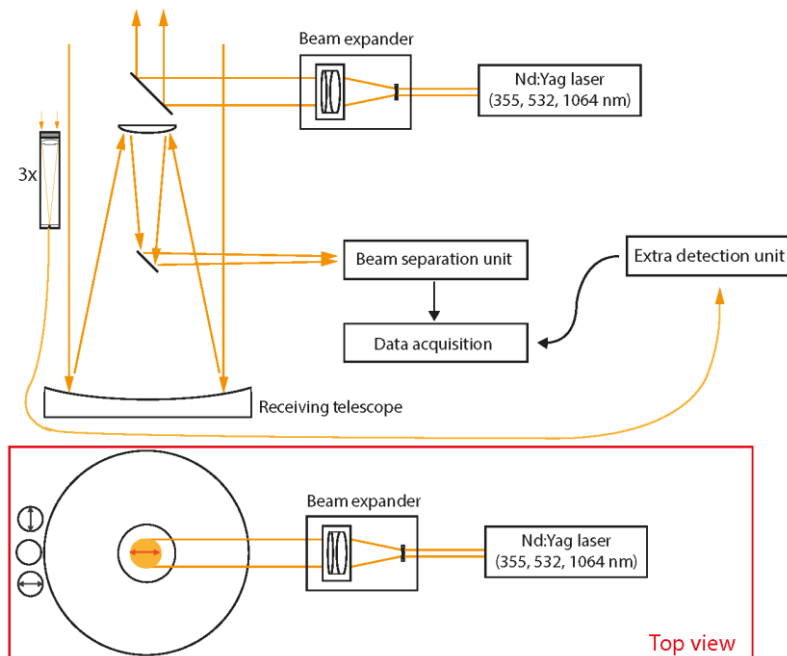
Figure 1: Overview of the EARLINET lidar MARTHA. The three-signal receiver unit of the new polarization lidar setup (details are shown in Fig. 2) is integrated into the MARTHA telescope construction (left side in both of the two sketches). The outgoing laser beam is 54 cm away from the new polarization-sensitive receiver unit. The main plane of linear polarization of the laser pulses and

10 **the polarization sensitivity of cross- and co-polarized receiver channels are indicated by arrows in the top-view sketch.**

Figure 2 provides details of the new polarization-sensitive channels. Each of the small receiver telescopes consist of 2" (50.8 mm) achromatic lens with a focal length of 250 mm. An optical fiber with an aperture of 400 µm is placed at the focal point of the lens. The resulting field of view (FOV) is 1.6 mrad. The receivers have in principle the same overlap function, since

15 they are identical and are implemented into the large telescope at the same distance from the laser beam axis. The laser-beam receiver-FOV overlap (obtained theoretically) is complete at about 650 m above the lidar (Stelmaszczyk et al., 2005).

At the output of the fiber a 2 mm ball lens is placed (scrambler in Fig. 2) in order to remove the small sensitivity of the interference filter to the changing incidence angle of backscattered light in the near-range. Only above 650 m (full overlap), we can assume that all light from all heights is backscattered at exactly 180°. A spatial attenuation unit which consists of two

20 optical fibers is integrated in the receiver setup, replacing the usual setup with neutral density filters. The distance between the

two fibers with given aperture can be changed and thus the strength of the incoming lidar return signal. The attenuation factor depends on the square of the distance between the fibers and on the numerical aperture of the fibers. E.g., signal attenuation by a factor of about 100 when the distance is 25 mm, and about 1000 with 79 mm distance.

The purpose of the new receiver system is to measure accurate profiles of the volume depolarization ratio in clouds between 1 and 12 km height. For the separation of the polarization components two of the three polarization telescopes are equipped with a linear polarization filter (see Fig. 2, linear polarizer) in front of the entrance lens. In the alignment process, the cross-polarized axis is found when the count rates are at the minimum. The co-polarized channel is then rotated by 90° compared to the cross-polarized filter position, because it is set manually, the difference between the true polarization axis of the filters may not be 90°, however, in this approach we will assume it, since the impact of small variations in the pointing angles of the polarization filters can be neglected (see Appendix A). Additionally, a small tilt between the finally obtained polarization plane of the receiver unit and the true polarization state (main plane of linear polarization) of the transmitted laser pulses is expected and thus assumed in the methodology outlined in Sect. 3.
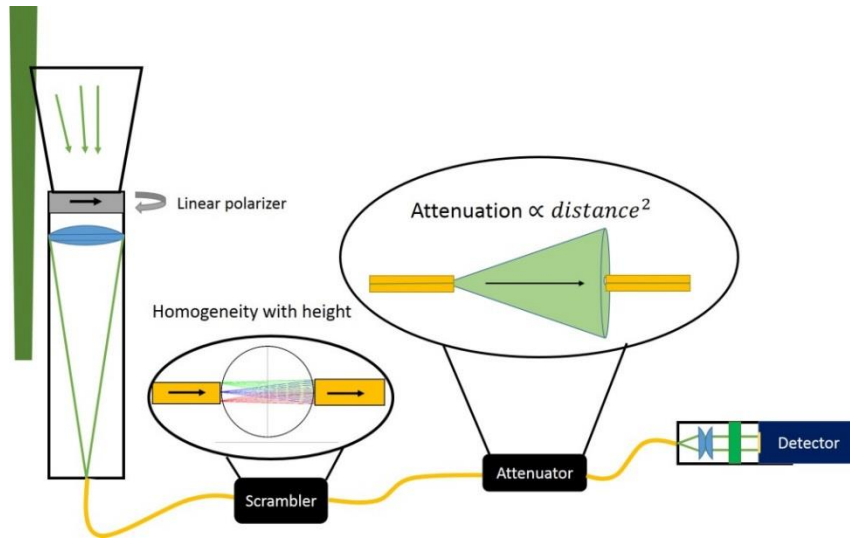
Figure 2: Sketch of one of the three identical receiver channel of the three-signal polarization lidar. The different parts are explained in the text.

3 Methodology

In Sect. 3.1, we begin with definitions and equations that allow us to describe the transmission of polarized laser pulses into the atmosphere, backscatter, extinction, and depolarization of polarized laser radiation by the atmospheric constituents, and the influence of the receiver set up on the depolarization ratio measurements. As first step in this theoretical framework we

will derive three lidar equations for our three measured signal components. In Sect. 3.2, we then present the derivation of the new three-signal method for the determination of the volume depolarization ratio starting from the three lidar equations (one for each channel) defined in Sect. 3.1.

3.1 Theoretical background: Three-signal polarization lidar

5 We follow the explanations and part of the notation of Freudenthaler (2016), Bravo-Aranda et al. (2016), and Belegante et al. (2018) in the description of the lidar setup, from the laser source (as part of the transmitter unit) to the detector unit (as part of the receiver block), and regarding the interaction of the polarized laser light photons with atmospheric particles and molecules by means of the Müller- Stokes formalism (Chipman, 2009). A Stokes vector describes the flux and the state of polarization of the transmitted laser radiation pulses and Müller matrices describe how the optical elements of the transmitter and receiver

10 units and the atmospheric constituents change the Stokes vector. The laser beam is expanded before transmission into the atmosphere. In most polarization lidar applications it is assumed that the transmitted laser radiation is totally linearly polarized. But this is not the case in practice. In our approach, we therefore take into consideration that the transmitted wave front contains a non-negligible, small amount of cross-polarized light after passing through the beam expander. Additionally, we consider a small-angular misalignment, described by angle α between the main plane of polarization of the laser beam and the

15 orientation of the respective plane of polarization defined by the polarization filters in front of the telescopes of the receiver unit of our three-channel polarization lidar configuration described below (these considerations can be visualized in Fig. 3).

The transmitted radiation $P_0(z)$ of the laser pulse can be written as the sum

$$P_0 = P_{0,II} + P_{0,\perp} \tag{1}$$

with the co- and cross-polarized light components, $P_{0,II}$ and $P_{0,\perp}$, with polarizations parallel and orthogonal to the main plane

20 of laser light polarization. We introduce the so-called crosstalk term ε_l,

$$\varepsilon_l = \frac{P_{0,\perp}}{P_{0,II}}, \tag{2}$$

which describes the small amount of cross-polarized light in the laser beam after leaving the transmission block of the lidar towards the atmosphere. Now we can write:

$$P_0 = (1 + \varepsilon_l)P_{0,II}. \tag{3}$$

25 The transmitted electromagnetic wave front is then given by the Stokes vector (Lu and Chipman, 2009)

$$\boldsymbol{I_L} = P_{0,II}\begin{pmatrix} 1+\varepsilon_l \\ 1-\varepsilon_l \\ 0 \\ 0 \end{pmatrix} = P_0\begin{pmatrix} 1 \\ \frac{1-\varepsilon_l}{1+\varepsilon_l} \\ 0 \\ 0 \end{pmatrix}. \tag{4}$$

The misalignment between the polarization axis of the transmitted light and the co-polarized receiver channel (defined by the respective polarization filter in front of the PMT) is characterized by angle α and described by the rotation Müller matrix (Bravo-Aranda et al., 2016), here we adopt the notation for the trigonometric functions used in (Freudenthaler, 2016), i.e.,

30 $\cos(2\alpha) := c_{2\alpha}$ and $\sin(2\alpha) := s_{2\alpha}$:

$$\mathbf{R(\alpha)} = \begin{pmatrix} 1 & 0 & 0 & 0 \\ 0 & \cos(2\alpha) & -\sin(2\alpha) & 0 \\ 0 & \sin(2\alpha) & \cos(2\alpha) & 0 \\ 0 & 0 & 0 & 1 \end{pmatrix} = \begin{pmatrix} 1 & 0 & 0 & 0 \\ 0 & c_{2\alpha} & -s_{2\alpha} & 0 \\ 0 & s_{2\alpha} & c_{2\alpha} & 0 \\ 0 & 0 & 0 & 1 \end{pmatrix} \tag{5}$$

Then the incident field after backscattering by atmospheric particles and molecules, and before passing the receiver block can be written as (Freudenthaler, 2016):

$$\boldsymbol{I_{in}} = \mathbf{FR(\alpha)}\boldsymbol{I_L} = F_{11} \begin{pmatrix} 1 & 0 & 0 & 0 \\ 0 & a & 0 & 0 \\ 0 & 0 & -a & 0 \\ 0 & 0 & 0 & 1-2a \end{pmatrix} \begin{pmatrix} 1 & 0 & 0 & 0 \\ 0 & c_{2\alpha} & -s_{2\alpha} & 0 \\ 0 & s_{2\alpha} & c_{2\alpha} & 0 \\ 0 & 0 & 0 & 1 \end{pmatrix} P_0 \begin{pmatrix} 1 \\ \frac{1-\varepsilon_l}{1+\varepsilon_l} \\ 0 \\ 0 \end{pmatrix} ,$$

$$\boldsymbol{I_{in}} = F_{11} P_0 \begin{pmatrix} 1 \\ \frac{1-\varepsilon_l}{1+\varepsilon_l} c_{2\alpha} a \\ -\frac{(1-\varepsilon_l)}{1+\varepsilon_l} s_{2\alpha} a \\ 0 \end{pmatrix} \tag{6}$$

with the atmospheric polarization parameter

$$a = \frac{1-\delta}{1+\delta}. \tag{7}$$

The scattering matrix $\mathbf{F}$ describes the interaction of the laser photons with the atmospheric particles and molecules. F_{11} and δ are the backscatter coefficient and the volume linear depolarization ratio, respectively.

The true volume backscatter coefficient ($\beta := F_{11}$) is given by

$$\beta = \beta_{II} + \beta_{\perp} = (1+\delta)\beta_{II} \tag{8}$$

with the backscatter contributions for the co- and cross-polarization planes (with respect to the true polarization planes given by the transmitted laser pulses). The volume linear depolarization ratio is defined as

$$\delta(z) = \frac{\beta_{\perp}(z)}{\beta_{II}(z)}. \tag{9}$$

Figure 3 illustrates the different polarization states and configurations of the original laser pulses (Fig. 3a) and after leaving the beam expander as elliptically polarized laser light (Fig. 3b). The receiver block may be not well aligned to the main plain of laser radiation so that the PMT measures different cross- and co polarized signal components with respect the outgoing cross- and co-polarized laser light components in Fig. 3b. The rotated polarization axis is represented in Fig. 3c, and after being backscattered and depolarized, the incident polarization plane has the form as shown in Fig. 3d.

To distinguish the apparent, measured volume backscatter coefficient, determined from the actually measured co- and cross-polarized signal components which are related to the incident field $\boldsymbol{I_{in}}$ (Eq. (6), see Fig. 3c) we introduce index 'in' and have the following relationships and links to the (true) laser light polarization plane:

$$\beta_{in} = \beta_{II,in} + \beta_{\perp,in} = \beta, \tag{10}$$

$$\beta_{II,in} - \beta_{\perp,in} = \frac{1-\varepsilon_l}{1+\varepsilon_l} c_{2\alpha} a\beta. \tag{11}$$
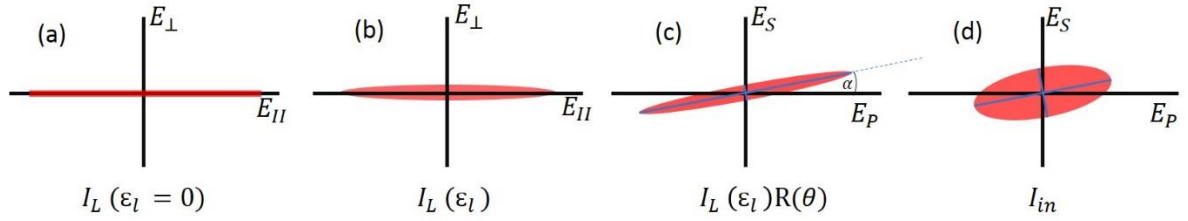
Figure 3: (a) Polarization state of the light generated by the laser (100% linearly polarized), E denotes electromagnetic field. **(b)** The laser radiation is elliptically polarized after passing the beam expander (see Fig. 1). **(c)** The receiving cross- and co-polarized signal channels (E_S and E_P) are usually not perfectly aligned to the main polarization plane of the laser radiation, i.e. $\alpha > 0$. **(d)** Polarization plane in the receiver for light which has been backscattered and depolarized by the atmosphere.

Using now Eq. (10) (describing the first term of I_{in} in Eq. (6)) and Eq. (11) (describing the second term of I_{in} in Eq. (6)), the apparent backscatter components $\beta_{II,in}$ and $\beta_{\perp,in}$ can be written as:

$$\beta_{II,in} = \left(1 + \frac{(1-\delta)}{(1+\delta)}\frac{(1-\varepsilon_l)}{(1+\varepsilon_l)}c_{2\alpha}\right)\beta/2, \tag{12}$$

$$\beta_{\perp,in} = \left(1 - \frac{(1-\delta)}{(1+\delta)}\frac{(1-\varepsilon_l)}{(1+\varepsilon_l)}c_{2\alpha}\right)\beta/2 . \tag{13}$$

These three backscattering components (Eqs. (10), (12), and (13)) can be measured separately using the three different telescopes of our polarization lidar described in Sect. 2.

It is worthwhile to mention that polarization lidars typically have two detection channels, either a cross-polarized and a parallel-polarized channel or a cross-polarized and so-called total channel. A commonly used method for the calibration is to insert an additional polarization filter into the optical path of the receiver unit and to rotate or tilt a $\lambda/2$ plate (Liu and Wang, 2013; Engelmann et al., 2016, McCullough et al., 2017). For these calibrations an extra measurement period is required. This calibration can introduce new and significant uncertainties (Biele et al., 2000; Freudenthaler et al., 2009; Mattis et al., 2009; Haarig et al., 2017).

As mentioned in the introduction, the concept to calibrate a lidar depolarization receiver by using three channels was proposed by Reichardt et al. 2003. The method consists of an absolute calibration procedure based on the measurement of elastically backscattered light with three detection channels for measuring co-, cross- and totally polarized backscatter components.

To determine the number of counts that the detection channels measure, Müller matrices representing the optical path of each channel would need to be added on Eq. (6). Nevertheless, in this approach we follow the view adopted by Reichardt et al. (2003), where the traditional lidar equation is used to characterize the lidar channels.

Let us now introduce the lidar equations for these three signals. Following Reichardt et al. (2003), the number of photons N_i that a lidar detects at height z (above the full overlap height) with channel i is given by

$$N_i(z) = P_0\left(\eta_{II,i}\beta_{II,in}(z) + \eta_{\perp,i}\beta_{\perp,in}(z)\right)T^2(z)/z^2 . \tag{14}$$

P_0 is the number of emitted laser photons and $\eta_{II,i}$ and $\eta_{\perp,i}$ are the optical efficiencies regarding the co- and cross-polarized components ($\beta_{II,in}$ and $\beta_{\perp,in}$) of the backscattered light that arrives at the channel-i detector. These efficiencies include instrumental constants that contain the total transmittance through all optical components and gain of the detectors and attenuation in the path of each channel. T denotes the atmospheric single-path transmission and is the same for all three detection channels (co, cross and total), since the extinction is independent of the state of polarization of the light. Rearrangements lead to the following versions of the lidar equations for the cross (S) and co-polarized (P) channels:

$$N_i(z) = P_0\, \eta_{II,i} \left(\beta_{II,in}(z) + D_i\beta_{\perp,in}(z)\right) T^2(z)/z^2, \tag{15}$$

or

$$N_i(z) = P_0\, \eta_{\perp,i} \left(D_i^{-1}\beta_{II,in}(z) + \beta_{\perp,in}(z)\right) T^2(z)/z^2, \tag{16}$$

here D_i denotes the so-called efficiency ratio (Reichardt et al., 2003), and it is defined as:

$$D_i := \frac{\eta_{\perp,i}}{\eta_{II,i}}, \tag{17}$$

The absence of optical elements before the polarization filters (such as the telescope itself and beamsplitters) avoids further polarization effects, such as diattenuation and retardation (Freudenthaler, 2016). Moreover, since we employed the same filter model in the optical path of the channels P and S, we assumed that $D_P = D_S^{-1}$. In the case of the total signal component ($i=$ tot) we assume that $D_{tot} = 1$ and we introduce the overall efficiency η_{tot} for simplicity reasons. The numbers of photons measured with each of the three channels (i = P, S, tot) are then given by

$$N_P(z) = P_0\eta_{II,P} \left(\beta_{II,in}(z) + D_P\beta_{\perp,in}(z)\right) T^2(z)/z^2, \tag{18}$$

$$N_S(z) = P_0\eta_{\perp,S} \left(\beta_{\perp,in}(z) + D_S^{-1}\beta_{II,in}(z)\right) T^2(z)/z^2, \tag{19}$$

$$N_{\text{tot}}(z) = P_0\eta_{tot}\beta_{in}(z)T^2(z)/z^2. \tag{20}$$

After further rearranging we finally obtain:

$$\frac{N_P(z)z^2}{\eta_{II,P}P_0T^2(z)} = \beta_{II,in}(z) + D_P\beta_{\perp,in}(z), \tag{21}$$

$$\frac{N_S(z)z^2}{\eta_{\perp,S}P_0T^2(z)} = \beta_{\perp,in}(z) + D_S^{-1}\beta_{II,in}(z), \tag{22}$$

$$\frac{N_{tot}(z)z^2}{\eta_{tot}P_0T^2(z)} = \beta_{in}(z). \tag{23}$$

To consider, in the next step, receiver misalignment and crosstalk effects, we introduced the parameters $\varepsilon_l = \frac{P_{0,\perp}}{P_{0,II}}$ (Eq. (2)), describing the small amount of cross-polarized light in the laser beam after leaving the transmission block into the atmosphere, and the rotation angle α, describing the angular misalignment between the transmitter and receiver units. To consider also the receiver-channel crosstalk, we further introduce ε_r, defined by $\varepsilon_r = D_S^{-1} = D_P$. The receiver crosstalk value is typically $\varepsilon_r \leq 10^{-3}$ (according to the filter manufacturer) as here the only element to consider is the polarization filter in front of the telescopes. Combining now Eqs. (10), (12), and (13) with Eqs. (21) - (23), we can write:

$$\frac{N_P(z)z^2}{\eta_{II,P}P_0T^2(z)} = \beta_{II,in}(z) + \varepsilon_r\beta_{\perp,in}(z) = \left(1 + \varepsilon_r + \frac{(1-\delta(z))}{(1+\delta(z))}\frac{(1-\varepsilon_l)}{(1+\varepsilon_l)}(1 - \varepsilon_r)c_{2\alpha}\right)\beta(z)/2, \tag{24}$$

$$\frac{N_S(z)z^2}{\eta_{\perp,S}P_0T^2(z)} = \beta_{\perp,in}(z) + \varepsilon_r\,\beta_{II,in}(z) = \left(1 + \varepsilon_r - \frac{(1-\delta(z))}{(1+\delta(z))}\frac{(1-\varepsilon_l)}{(1+\varepsilon_l)}(1 - \varepsilon_r)c_{2\alpha}\right)\beta(z)/2, \tag{25}$$

$$\frac{N_{tot}(z)z^2}{\eta_{tot}P_0T^2(z)} = \beta_{in}(z) = \beta(z). \tag{26}$$

Until this point, the analytical procedure has been based on the assumption that the polarization filters in front of the cross- and co-polarized telescopes are pointing 90° with respect to each other. However, in the general case, when their angular deviation with respect to their respective components is different (E_P to E_{II} and E_S to $E_\perp$), Eqs. (24) and (25) have a different angular component. In this approach, we keep this assumption for the development of a simple calibration procedure. In Appendix A, the general case is evaluated (angle P to S $\neq$ 90°), and based on a measurement example, we demonstrated that the impact of this assumption can be neglected in our system.

3.2 Determination of calibration constants and the volume linear depolarization ratio

Outgoing from Eqs. (24)-(26) we will define instrumental (inter-channel) constants which are required to calibrate the lidar in the experimental practice and which are also used in the determination of the volume linear depolarization ratio. The equations for the determination of the depolarization ratios will be given. Three different ways can be used to determine the linear depolarization ratio profiles.

Considering Eq. (26) and the sum of Eqs. (24) and (25), we can write

$$\frac{N_{tot}(z)}{\eta_{tot}} = \frac{1}{1+\varepsilon_r}\left(\frac{N_P(z)}{\eta_{II,P}} + \frac{N_S(z)}{\eta_{\perp,S}}\right), \tag{27}$$

Eq. (27) is independent of the transmission crosstalk factor ε_l and of the rotation of the receiver axis (and thus rotation angle α), but depends on the receiver crosstalk factor ε_r.

Let us introduce the following inter-channel instrumental constants

$$X_P = \frac{\eta_{tot}}{(1+\varepsilon_r)\eta_{II,P}}, \tag{28}$$

$$X_S = \frac{\eta_{tot}}{(1+\varepsilon_r)\eta_{\perp,S}}, \tag{29}$$

$$X_\delta = \frac{\eta_{II,P}}{\eta_{\perp,S}} = \frac{X_S}{X_P} \tag{30}$$

and the signal ratios R_P, R_S, R_δ

$$R_P(z) = \frac{N_P(z)}{N_{tot}(z)}, \tag{31}$$

$$R_S(z) = \frac{N_S(z)}{N_{tot}(z)}, \tag{32}$$

$$R_\delta(z) = \frac{N_S(z)}{N_P(z)}. \tag{33}$$

By using these definitions, Eq. (27) (after multiplication with $\frac{\eta_{tot}}{N_{tot}(z)}$) can be rearranged to

$$X_P R_P(z) + X_S R_S(z) = 1. \tag{34}$$

Eq. (34) is only valid for the case of an almost ideal polarization lidar receiver unit, i.e., when $D_S^{-1} = D_P$ ($= \varepsilon_r$). This is not the case for most of lidar systems where the receiver and separation unit may introduce differences between the transmission ratios D_S^{-1} and D_P. In the next step, we form the difference of Eq. (34) for altitude z_j minus Eq. (34) for altitude z_k and obtain:

$$X_\delta(z_j, z_k, t) = -\frac{R_P(z_j,t) - R_P(z_k,t)}{R_S(z_j,t) - R_S(z_k,t)}, \tag{35}$$

in the same way, when Eq. (27) is multiplied by $\frac{\eta_{\perp,S}}{N_S(z)}$ and $\frac{\eta_{II,P}}{N_P(z)}$, we can derive Eqs. (36) and (37) respectively.

$$X_S(z_j, z_k, t) = \frac{R_P^{-1}(z_j,t) - R_P^{-1}(z_k,t)}{R_\delta(z_j,t) - R_\delta(z_k,t)}, \tag{36}$$

$$X_P(z_j, z_k, t) = \frac{R_S^{-1}(z_j,t) - R_S^{-1}(z_k,t)}{R_\delta^{-1}(z_j,t) - R_\delta^{-1}(z_k,t)} \tag{37}$$

t denotes time.

In the conventional 3-signal calibration approach, each signal is normalized to a reference altitude, by doing so the efficiencies of the three channels $\eta_{II,P}$, $\eta_{\perp,S}$ and η_{tot} cancel themselves from the equations, then the ratios between the three normalized signals are calculated. The retrieval of the volume depolarization ratio is done by solving a system of two equations and two unknowns: the volume depolarization ratio at a reference height $\delta(z_0)$ and the volume depolarization ratio at all heights $\delta(z)$ (Reichardt et al., 2003).

In this extended 3-signal calibration procedure, the signals are not normalized to a reference height z_0, instead, we divide directly the signals, obtaining the ratios R_P, R_S and R_δ, by taking then the difference between two altitudes (and not the ratio) we subtract the crosstalk in the emission and reception (ε_l and ε_r) and the angular misalignment ($c_{2\alpha}$). The difference offers additionally a better performance in terms of error propagation compared to the ratio. In this way, the so called interchannel constants (X_δ, X_S and X_P) remain in the equations and they can be estimated by evaluating Eqs. (35), (36) and (37) respectively. Although we can estimate this three constants, we have to note that the number of unknowns are actually two X_P and X_S being the third constant X_δ the ratio of them (please see Eq. (30)), i.e. Eq.(35) is equivalent to Eq.(36) divided Eq. (37).

Given the form of Eqs. (35)-(37), observable differences between the height points z_j and z_k are needed for its evaluation, in practice, only altitude regions should be selected in the determination of X_P, X_S, and X_δ where significant changes in the depolarization ratio occur, e.g., in liquid-water clouds where multiple scattering by droplets produce steadily increasing depolarization with increasing penetration of laser light into the cloud (Donovan et al., 2015; Jimenez et al., 2017; Jimenez et al., 2018). Long measurements periods should be considered for the evaluation of Eqs. (35)-(37). All pair of data points (z_j and z_k in a certain height range, defined according to the ratio of signals) in all single measurements (in time t) provide an array with many observations of the interchannel constants, averaging these arrays we obtain a trustworthy estimate of these constants for the retrieval of the volume depolarization ratio (please see Figure 6).

To derive the linear depolarization ratio, we divide Eq. (25) by Eq. (24),

$$\frac{N_S}{N_P}\frac{\eta_{II,P}}{\eta_{\perp,S}} = X_\delta R_\delta = \frac{(1+\varepsilon_r)(1+\varepsilon_l)-\frac{(1-\delta)}{(1+\delta)}(1-\varepsilon_l)(1-\varepsilon_r)c_{2\alpha}}{(1+\varepsilon_r)(1+\varepsilon_l)+\frac{(1-\delta)}{(1+\delta)}(1-\varepsilon_l)(1-\varepsilon_r)c_{2\alpha}}. \tag{38}$$

Furthermore, we introduce the total crosstalk factor ξ_{tot},

$$\xi_{tot} = \frac{(1+\varepsilon_r)(1+\varepsilon_l)}{(1-\varepsilon_l)(1-\varepsilon_r)c_{2\alpha}} \geq 1, \tag{39}$$

which takes account for the combined effect of the emitted elliptically polarized wave front ε_l, of the angular misalignment between emitter and receiver (described by the rotation angle α), and of the crosstalk between receiver channels described by ε_r. The factor ξ_{tot} would be equal to 1 if the emitted laser pulses are totally linearly polarized, misalignment of the receiver unit could be avoided, and crosstalk between receiver channels are negligible.

Now Eq. (38) can be rewritten after dividing the numerator and denominator by $(1-\varepsilon_l)(1-\varepsilon_r)c_{2\alpha}$ and rearranging the equation:

$$X_\delta R_\delta = \frac{\xi_{tot}-\frac{(1-\delta)}{(1+\delta)}}{\xi_{tot}+\frac{(1-\delta)}{(1+\delta)}} \tag{40}$$

and the volume depolarization ratio can be obtained from Eq. (40) after rearrangement,

$$\delta(R_\delta, X_\delta, \xi_{tot}) = \frac{1-\xi_{tot}+X_\delta R_\delta(1+\xi_{tot})}{1+\xi_{tot}+X_\delta R_\delta(1-\xi_{tot})}. \tag{41}$$

As shown in Eq. (41), the volume depolarization ratio can be calculated by using the ratio R_δ between the cross and co-polarized signals and when the constants X_δ and ξ_{tot} are known. As first step of the calibration, the inter-channel constant X_δ (together with X_P and X_S) is obtained from the measurements by evaluating Eqs. (35)-(37) in the selected height range (with variations on the depolarization) at each measurement time t. Then ξ_{tot} can be estimated in a region (defined by height z_{mol}) with dominating Rayleigh backscattering for which the volume depolarization ratio, δ_{mol}, is assumed as constant and known.

Behrendt et al. (2002) estimated theoretically a value of the linear depolarization ratio caused by molecules of 0.0046 for a lidar system whose interference filters have a FWHM=1.0 nm, however, Freudenthaler et al. (2016b) has found a value of 0.005 ± 0.012 based on long-term measurements in aerosol and cloud-free tropospheric height regions. We used this value and we have considered the propagation of this systematic uncertainty in our calculations. From, Eq. (41) ξ_{tot} is given by.

$$\xi_{tot} = \left(\frac{1-\delta_{mol}}{1+\delta_{mol}}\right)\left(\frac{1+X_\delta R_\delta(z_{mol})}{1-X_\delta R_\delta(z_{mol})}\right), \tag{42}$$

By calculating the ratio between Eqs. (24) and (26) (co to total) or the ratio between Eqs. (25) and (26) (cross to total), the volume depolarization ratio can also be derived:

$$\delta(R_S, X_S, \xi_{tot}) = \frac{1-\xi_{tot}(1-2X_S R_S)}{1+\xi_{tot}(1-2X_S R_S)}, \tag{43}$$

$$\delta(R_P, X_P, \xi_{tot}) = \frac{1-\xi_{tot}(2X_P R_P-1)}{1+\xi_{tot}(2X_P R_S-1)}. \tag{44}$$

In summary, the volume linear depolarization ratio can be calculated after the determination of the constants X_P, X_S, X_δ and

ξ_{tot}. Then the signal ratio profiles $R_P(z)$, $R_S(z)$, and $R_\delta(z)$ are required and calculated within Eqs. (31), (32) and (33), and by considering Eqs. (41), (43) and (44) the depolarization ratio can be finally calculated by using either the pair of signals N_S and N_P, the pair N_S and N_{tot}, or the pair N_P and N_{tot} respectively. However, the expected errors in the retrievals are not the same for all this pairs, since they present different sensitivities to changes in the depolarization ratio, obtaining the largest

5 uncertainties when the pair N_P and N_{tot} is used.

4 Observations

4.1 Application of the calibration approach to a measurement case

To test the method introduced in Sect. 3, the measurement case from 19 September 2017 was analyzed and the results are presented in this section. Figure 4 provides an overview of the atmospheric situation. An aerosol layer reached up to about 2.8

10 km height and was topped by a persistent, shallow altocumulus deck with cloud base height at 2.6-2.7 km a.g.l. (above ground level)

Although the time resolution of the lidar measurements is 30 seconds, to reduce computing time and signal noise, we consider 5 minutes average measurements. Figure 5 shows as example the three range-corrected signals of the polarization lidar, the signal ratios as defined by Eqs. (31)-(33), and the corresponding inverse ratios for a 5-minute measurement.
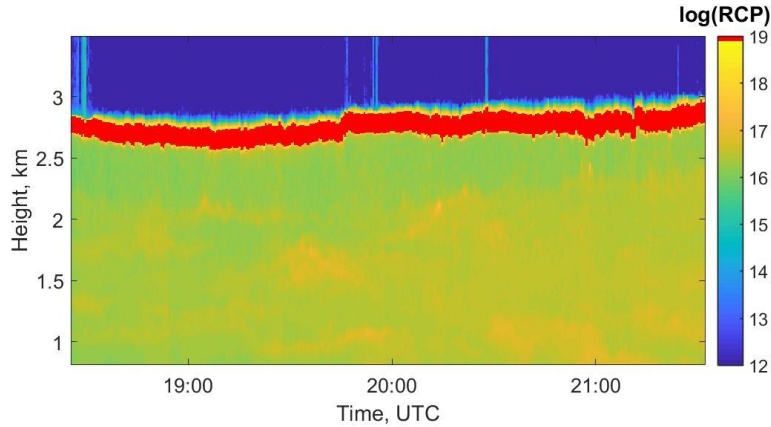
Figure 4: Range-corrected 532 nm total backscatter signal (RCP) measured on 19 September 2017 with 30 s and 7.5 m vertical resolution.

In the next step of the data analysis and calibration procedure, we selected the height range from a few meters below cloud base up to 240 meters above cloud base for each 5-minute averaging period t, then we computed the instrumental inter-channel

20 ratios $X_P(z_j, z_k, t)$, $X_S(z_j, z_k, t)$, and $X_\delta(z_j, z_k, t)$ with Eqs. (37), (36), and (35), respectively. Height resolution was 7.5 m. The result is shown in Fig. 6.
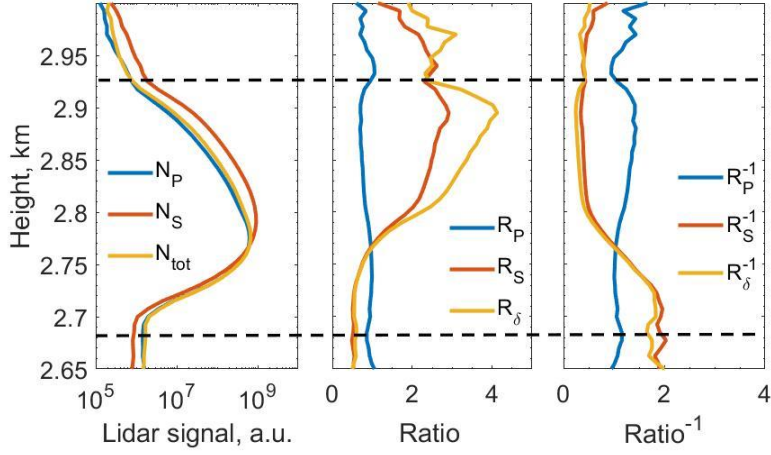
Figure 5: Example of a 5-minute profile of range-corrected lidar signals from the channels, signal ratios, and inverse ratios. The calibration procedure considers all signals of the 3-hour measurement period shown in Fig. 4. The dash line indicates the range where the calibration calculations where done.
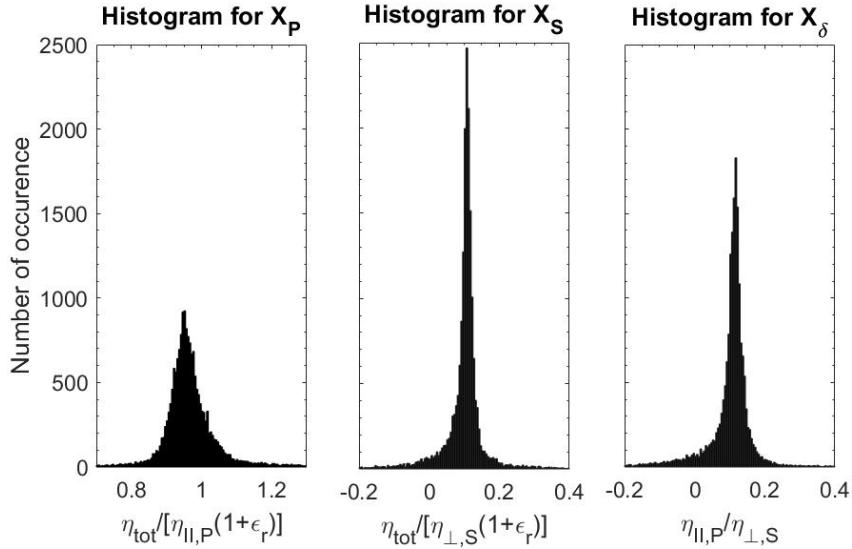
Figure 6: Histograms for the inter-channel constants X_P, X_S and X_δ. Each point corresponds to a combination z_j and z_k in a 5-minute period, obtaining about 18000 data points for this 3-hour measurement case.

The mean values of the constants with the respective statistical error based on Fig. 6 are: $X_P = 0.965 \pm 0.012$, $X_S = 0.108 \pm 0.005$ and $X_\delta = 0.110 \pm 0.006$. The reason for these low uncertainties is that the calibration is performed in a cloudy region so that every channel shows high count rates and thus high signal-to-noise ratios.

Using the constant X_δ and evaluating Eq. (42) in the particle-free region of the 3-hour measurement period, a mean value of $\xi_{tot} = 1.118 \pm 0.008$ for the total crosstalk was obtained. Given the form of the equations to retrieve the profiles of volume depolarization ratio (Eqs. (35)-(37)), the propagated uncertainty associated to ξ_{tot} does not vary largely with height, which leads to a large percentage uncertainty on the retrieval of the volume linear depolarization ratio in the region with low depolarization ratios, also characterized by low signal strengths. Table 1 summarize the retrieved instrumental constants for the measurement case presented.

Table 1: Values of the instrumental inter-channel constants and crosstalk factor determined for the measurement case presented.

Instrumental constant	Value
X_P	0.965 ± 0.012
X_S	0.108 ± 0.005
X_δ	0.110 ± 0.006
ε_{tot}	1.118 ± 0.008

Figure 7 presents the height profiles of the volume linear polarization ratio computed by means of Eqs. (41), (43), and (44). Good agreement between the different solutions is visible. However, the depolarization ratios obtained from the channels N_P and N_{tot} (blue) shows the largest uncertainties, especially above the cloud layer. The profile-mean absolute uncertainties from the ground up to the cloud top (3.1 km) for $\delta(R_P, X_P)$, $\delta(R_S, X_S)$ and $\delta(R_\delta, C)$ are 0.034, 0.0139 and 0.0137, respectively. The three derived depolarization ratios agree well in the cloud region, differences appear in the upper part of the cloud caused by strongly reduced count rates due to the strong attenuation of all the channels, in order to avoid signal saturation at low level clouds.

Figure 8 presents the volume depolarization ratio with 30 s temporal resolution. The signal ratio R_δ and the constant X_δ where used. These profiles are the basis for the retrieval of the microphysical properties of the liquid-water cloud. The results will be discussed in a follow-up article (Jimenez et al., 2018b).
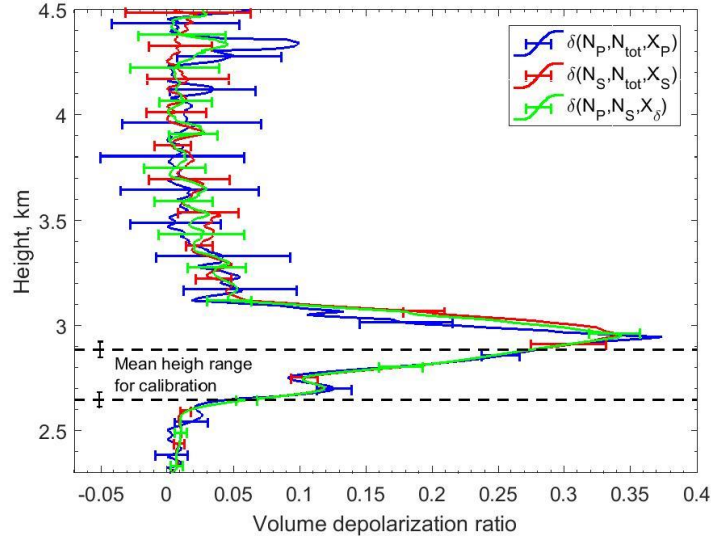
Figure 7: Profiles of the volume linear depolarization ratio for the 3 hours period in the cloud region, using the three pairs of signal ratios presented in Eqs. (41), (43) and (44). The error bars include the statistical and systematical uncertainties. The dash lines indicate the mean height range (of 240 meters) where the calculation of the interchannel constants was performed.
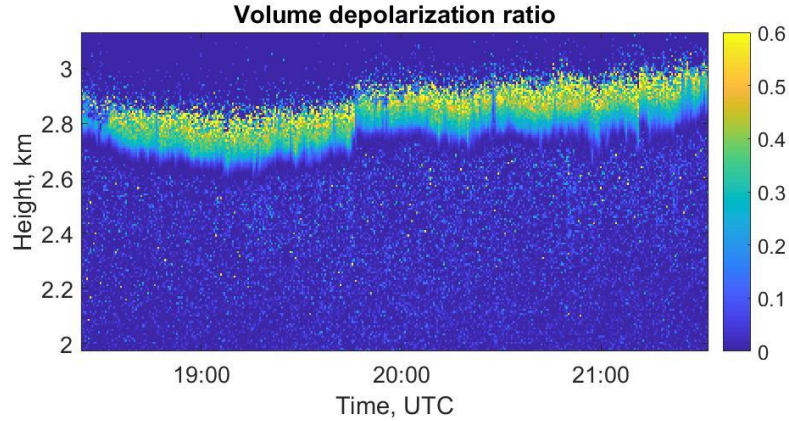
Figure 8: Volume linear depolarization ratio for the entire 3-hour period, shown in Fig. 4. The temporal resolution is 30 seconds.

To validate the new system and the calibration procedure a comparison between the measurements of the volume linear
10 depolarization ratio with the lidar systems MARTHA and BERTHA (Backscatter Extinction Lidar Ratio Temperature and Humidity profiling Apparatus) is presented in Figure 9. The observations were conducted at Leipzig (51°N, 12°E) on 29 May 2017 with the presence of a Dust layer between 2 and 5 km and a cirrus cloud at 11 km (see Fig. 9a). Good agreement in the dust layer can be noted, while the cirrus cloud shows differences between the two systems, that difference can be attributed to the fact that the BERTHA system is pointing 5° respect to the zenith, while the MARTHA system points to the Zenith (0°).

This could lead to specular reflection by horizontally oriented ice crystals reducing the depolarization ratio in the case of the MARTHA system.

A second measurement period during an unique event with a dense biomass burning smoke layer in the stratosphere on 22 August 2017 was considered for comparison (Haarig et al., 2018), here very good agreement for the layer between 5 and 7 km and also for the layer at 14 km was obtained, confirming the good performance of the systems and of the respective calibration procedures, extended 3-signal method in MARTHA and the Δ90° method in the BERTHA system.
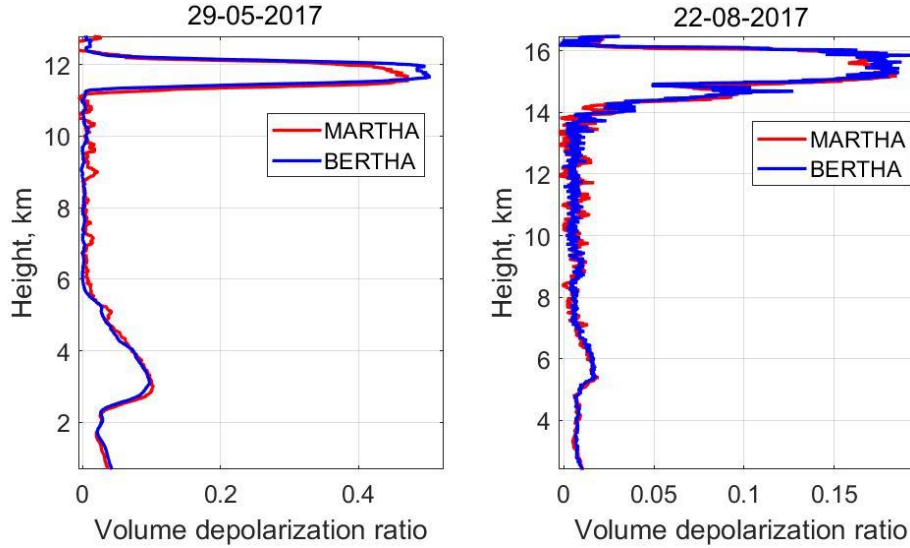
Figure 9: Volume linear depolarization ratio obtained with MARTHA (extended 3-signal method) and BERTHA (Δ90° method) on (a) 29 May 2017 20:20-20:45 (with smooth 27 bins) (b) 22 August 2017 20:45-23:15 (Haarig et al., 2018). The systems were calibrated independently. The system were located at a distance of 80 meters.

4.2 Temporal stability of the polarization lidar calibration and performance

The time series of the inter-channel constant X_δ obtained from MARTHA observations between day 120 and 320 of 2017 is presented in Fig. 10. The respective time series of ξ_{tot} is given in Fig. 11. As can be seen, the calibrations values show the lowest uncertainties in the inter-channel constants (of about 4%) when altocumulus layers with a stable cloud base and moderate light extinction were present. Higher uncertainty levels were observed in the case of cirrus clouds (green, 11%) and the Saharan dust layer. In the case of very thick cumulus clouds (black), the mean uncertainty was 21%. One reason for these differences in the uncertainty of X_δ is that the system was optimized for the observation of low-altitude liquid-water clouds, for which the detection channels need large attenuation to avoid saturation of the detectors in the cloud layer. This setup prohibited an optimum detection of high-level dust layers and ice clouds due to the low signal strength for these cases. Furthermore, liquid clouds are favorable for calibration because the volume depolarization ratio increases very smoothly as a

result of the increasing multiple scattering impact. At these conditions, a large number of measurement pairs for heights z_j and z_k with different depolarization ratios are available. Some slight changes of X_δ occurred when the attenuation configuration of the polarization receivers was changed. Small day-to-day changes were caused by small variations in the response of each detector with time.

5   In Fig. 10 are the retrieved values of ξ_{tot}, small variations can be seen but they remain much lower than the uncertainties, and no stronger variations can be noted with changes in the attenuation or changes of the calibration medium (water cloud, cirrus, Saharan dust layer). In 2017, the mean value $\xi_{tot} = 1.109 \pm 0.009$.
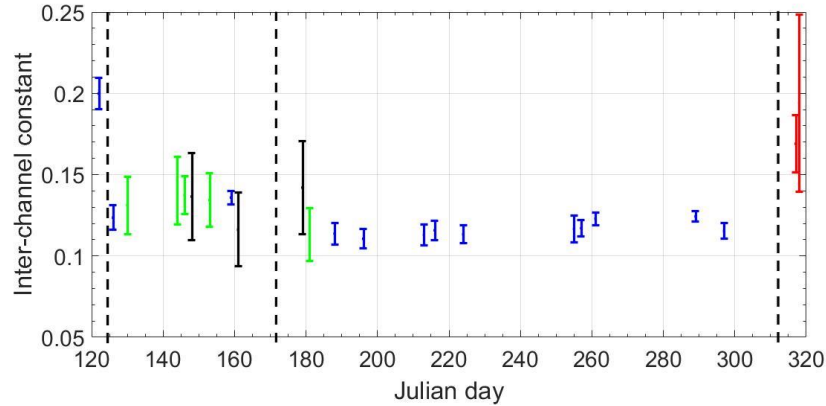
Figure 10: Time series of the inter-channel calibration constant X_δ measured from end of April to mid November 2017. The vertical
10   **bars show the uncertainty in the retrieval. The calibration procedure was based on lidar measurements in liquid-water clouds (blue), cirrus clouds (green), during optically thick cumulus events (black), and Saharan dust periods (red). The dash lines indicate the days where changes in the attenuation configuration of the channels were made.**
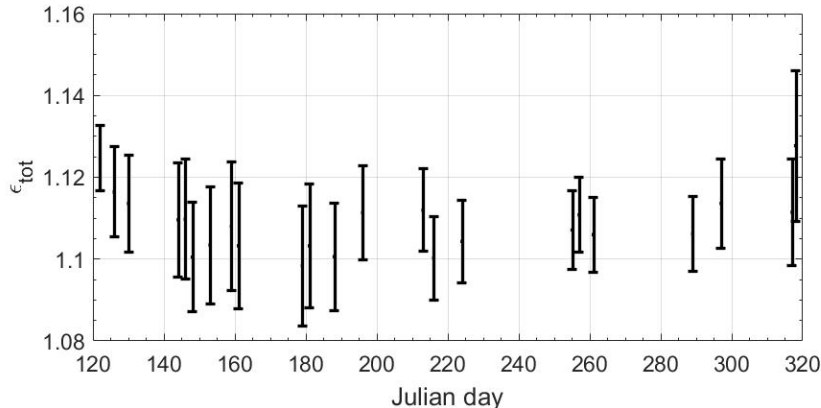
15   **Figure 11: Time series of the total crosstalk factor ε_{tot} measured in 2017. The vertical bars show the uncertainty in the retrieval, which include the statistical error from the determination of the inter-channel constants and systematical errors from the value considered in the molecular region 0.005 ± 0.0012.**

5 Summary and conclusions

In this work a new formalism to calibrate polarization lidar systems based on three detection channels has been presented. We propose a simple lidar polarization receiver, based on three telescopes (one for each channel) with a polarization filter on the front (in the case of the cross and co polarized channels), this set up removes the effect of the receiver optics on the polarization state of the collected backscattered light, simplifying the measurement concept. The derivation of the volume linear depolarization ratio considering the instrumental effects on the proposed system was described in Sect. 3, here there are three effects considered: the emitted laser beam (after beam expander) is slightly elliptically polarized (ε_l), there is an angular misalignment (α) of the receiver unit with respect to the main polarization plane of the emitted laser pulses and there is a small crosstalk amount in the detection channels (co and cross) (ε_r). These instrumental parameters can be summarized into one single constant, the so-called total crosstalk (ξ_{tot}).

The methodology does not require a priori knowledge about the behavior of the instrument in terms of polarization and permits the determination of the so-called inter-channel constants X_P, X_S and X_δ, which depend on the attenuation and detector response of each channel, and thus it is expected to vary between different measurement days. In the free-aerosol region the total crosstalk can also be estimated by means of long term measurements, in our case we estimated a mean value of $\xi_{tot} = 1.109 \pm 0.009$. The calibration is based on actual lidar measurement periods, providing large amount of input data for accurate estimation of the mean value of the instrumental constants. However, it needs a strong depolarizing medium for its application, such as dust layers and also water clouds, which depolarize the light due to multiple scattering in droplets or due to single scattering of ice particles.

A case study of a liquid-water cloud observation was presented, the 3-hours period demonstrates the potential of the new technique for the retrieval of accurate high temporal resolution depolarization profiles. The method is simple to implement and allows high quality depolarization ratio studies. Temporal studies indicated the robustness and stability of the three-signal lidar system over long time periods. A comparison with a second polarization lidar shows excellent agreement regarding the derived volume linear polarization ratio of biomass burning smoke throughout the troposphere and the lower stratosphere up to 16 km height.

Appendix A: General case regarding the rotation of the polarization filters with respect to the true polarization axis of the emitted light

For the derivation outlined in Sect. 3 it is assumed that the polarization filters in front of the cross- and co-polarized telescopes are pointing 90° with respect to each other. However, in the general case, when their angular deviation with respect to their respective components is different (E_P to E_{II} and E_S to $E_\perp$), Eqs. (24) and (25) have a different angular component. In this appendix we analyze this general case and discuss the need of implementation depending on the results obtained.

We define the angles α_P and α_S as the angular misalignment of the channels E_P and E_S with respect to E_{II} and $E_\perp$ respectively (see Fig A1). We rewrite Eqs. (24) - (26), we factorize by $(1 + \varepsilon_r)$ and to simplify the expression, we adopt the polarization parameter $a = \frac{(1-\delta)}{(1+\delta)}$ again. We do not use the short notation of the cosine adopted in Sect.3.
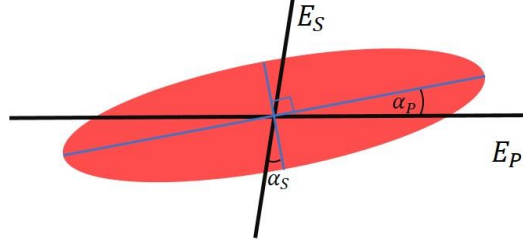
5   **Figure A1: Scheme of the observation of the polarization state of the backscattered light (similar to Fig. 3), the co and cross channels are misaligned with respect to their components in an angle α_P and α_S respectively.**

$$\frac{N_P(z)z^2}{\eta_{II,P}\,P_0 T^2(z)} = \beta_{II,in}(z) + \varepsilon_r \beta_{\perp,in}(z) = (1 + \varepsilon_r)\left(1 + a(z)\,\frac{(1-\varepsilon_l)}{(1+\varepsilon_l)}\frac{(1-\varepsilon_r)}{(1+\varepsilon_r)}\cos(2\alpha_P)\right)\beta(z)/2, \tag{A1}$$

$$\frac{N_\perp(z)z^2}{\eta_{\perp,S}P_0 T^2(z)} = \beta_{\perp,in}(z) + \varepsilon_r\,\beta_{II,in}(z) = (1 + \varepsilon_r)\left(1 - a(z)\,\frac{(1-\varepsilon_l)}{(1+\varepsilon_l)}\frac{(1-\varepsilon_r)}{(1+\varepsilon_r)}\cos(2\alpha_S)\right)\beta(z)/2, \tag{A2}$$

10   $$\frac{N_{tot}(z)z^2}{\eta_{tot}P_0 T^2(z)} = \beta_{in}(z) = \beta(z). \tag{A3}$$

In a similar way as we defined ξ_{tot}, we define the total crosstalk factor for the co and cross polarized channels respectively.

$$\xi_P = \frac{(1+\varepsilon_r)(1+\varepsilon_l)}{(1-\varepsilon_l)(1-\varepsilon_r)\cos(2\alpha_P)} \geq 1, \tag{A4}$$

$$\xi_S = \frac{(1+\varepsilon_r)(1+\varepsilon_l)}{(1-\varepsilon_l)(1-\varepsilon_r)\cos(2\alpha_S)} \geq 1, \tag{A5}$$

The three-signal polarization equation (Eq. (27)) can be rewritten in a general form, when adding Eqs. (A1) and (A2) and

15   considering Eq. (A3):

$$\left(\frac{N_P(z)}{\eta_{II,P}} + \frac{N_S(z)}{\eta_{\perp,S}}\right) = (1 + \varepsilon_r)(1 + a(z)(\xi_P^{-1} - \xi_S^{-1})/2)\frac{N_{tot}(z)}{\eta_{tot}}. \tag{A6}$$

The term $\xi_P^{-1} - \xi_S^{-1}$ depends on the difference of the cosines of $2\alpha_P$ and $2\alpha_S$, we define the parameter ξ_S^P which account for the difference of the impact of the polarization channels.

$$\xi_S^P := (\xi_P^{-1} - \xi_S^{-1})/2 = \frac{(1-\varepsilon_l)(1-\varepsilon_r)}{2(1+\varepsilon_l)(1+\varepsilon_r)}(\cos(2\alpha_P) - \cos(2\alpha_S))\,. \tag{A7}$$

20   This factor can be positive or negative, depending on which polarization filter is more misaligned, and it is equal to zero when they point 90° with respect to each other. Eq. (A6) can be expressed as:

$$\left(\frac{N_P(z)}{\eta_{II,P}} + \frac{N_S(z)}{\eta_{\perp,S}}\right) = (1 + \varepsilon_r)(1 + \xi_S^P a(z)\,)\frac{N_{tot}(z)}{\eta_{tot}}, \tag{A8}$$

We adopt the notation:

$$\Delta R_P(z_j\,, z_k) = R_P(z_j) - R_P(z_k), \tag{A9}$$

for account the difference between the signal ratios R_P, R_S and R_δ, between the polarization parameter a, and between the ratios a/R_S and a/R_P at the heights z_j and z_k. In an equivalent way as we derived Eqs. (35)-(37) we can obtain a general solution for the instrumental inter-channel constants:

$$X_P(z_j, z_k) = \frac{\Delta R_S^{-1}(z_k) + \xi_S^P \Delta\left(\frac{a}{R_S}(z_j, z_k)\right)}{\Delta R_\delta^{-1}(z_j, z_k)}, \tag{A10}$$

$$5 \quad X_S(z_j, z_k) = \frac{\Delta R_P^{-1}(z_j, z_k) + \xi_S^P \Delta\left(\frac{a}{R_P}(z_j, z_k)\right)}{\Delta R_\delta(z_j, z_k)}, \tag{A11}$$

$$X_\delta(z_j, z_k) = \frac{\Delta R_P(z_j, z_k) + \xi_S^P \frac{\Delta a(z_j, z_k)}{2X_P}}{\Delta R_S^{-1}(z_j, z_k)}, \tag{A12}$$

In an absolute sense it would not be possible to determine the inter-channel constants X_P, X_S and X_δ without knowing the polarization parameter (or the depolarization ratio), however, the impact on Eqs. (A10) - (A12) of their respective second term can be very small, since it depends on the difference of the cosines of small angles. For example, if $2\alpha_P = 5°$ and $2\alpha_S = 10°$,

10 using Eq. (A7) $\xi_S^P = 0.005 \frac{(1-\varepsilon_l)(1-\varepsilon_r)}{(1+\varepsilon_l)(1+\varepsilon_r)}$. Considering this small effect, a first guess of the polarization parameter would be sufficient to solve equations (A10) - (A12).

Calculating the three ratios between Eqs. (A1), (A2) and (A3), we can obtain the volume linear depolarization ratio, similarly as how it was done for Eqs. (41), (43) and (44).

$$\delta(R_S, X_S, \xi_S) = \frac{1 - \xi_S(1 - 2X_S R_S)}{1 + \xi_S(1 - 2X_S R_S)}, \tag{A13}$$

$$15 \quad \delta(R_P, X_P, \xi_P) = \frac{1 - \xi_P(2X_P R_P - 1)}{1 + \xi_P(2X_P R_P - 1)}, \tag{A14}$$

$$\delta(R_\delta, X_\delta, \xi_P, \xi_S) = \frac{1 + \frac{\xi_S}{\xi_P} X_\delta R_\delta - \xi_S(1 - X_\delta R_\delta)}{1 + \frac{\xi_S}{\xi_P} X_\delta R_\delta + \xi_S(1 - X_\delta R_\delta)}. \tag{A15}$$

$$a = \frac{1 - \delta}{1 + \delta}, \tag{A16}$$

In the measurement example presented, we performed an iterative computation procedure to determine the inter-channel calibration constants and the crosstalk factors. Using Eqs. (A10)-(A12), in a first run we determined the inter-channel constants

20 when we assume $\xi_S^P = 0$, i.e. $\theta_P = \theta_S$, a first guess of the volume depolarization ratio using each pair of signals is obtained (Eqs. (A13)- (A15)), then the corresponding crosstalks ξ_P and ξ_S are determined by imposing a mean value of $\delta = 0.005 \pm 0.012$ in the free aerosol region (Freudenthaler et al., 2016b). The second run takes the values of $\xi_S^P \neq 0$ and of the polarization parameter $a(z, t)$ (Eqs. (A14) and (A16)) from the first run and the inter-channel constants are computed again. Figure A2 shows the results of performing the calibration iteratively. Small differences between the values obtained in the first and second

25 run can be noted, in fact, the variations are smaller than the error of the respective constants, and we can see that after the second run, all values remain practically constant. The mean values of the instrumental constants after 6 iterations are listed in the Table A1.

In this measurement case we found a value for $\xi_S^P = -0.008$. Due to this small value there are no important variations between the first guess and the second run, therefore we conclude that by assuming $\xi_S^P = 0$ a fast and practical inversion procedure is possible. However, in cases with larger differences between α_P and α_S, an iterative procedure as described above would be needed.
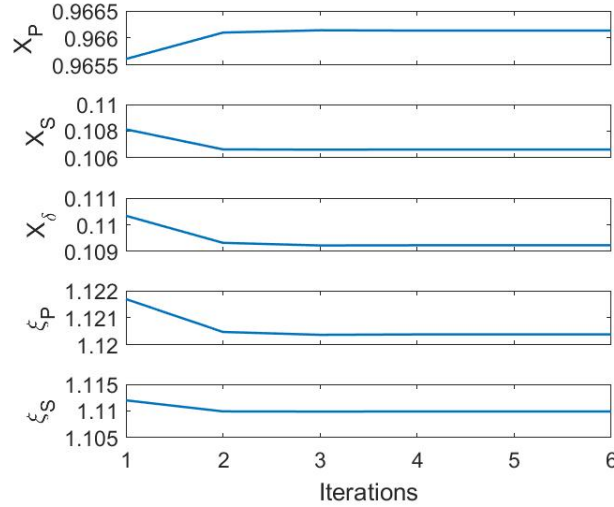
Figure A2: Instrumental channels obtained with an iterative procedure. We did not include the error bars since they are much larger than the variations between runs.

This general solution for the lidar three-signal problem converge to the same results when we also consider that the receiver crosstalk can be eventually different for the channels P and S. In that case we would have $\varepsilon_{r,P}$ and $\varepsilon_{r,S}$ which would also lead to two constants ξ_P and ξ_S to determine. For simplicity we talked in this section only about the effect of the different angular misalignment of the channel.

Table A1: Results of the instrumental constants after using the iterative procedure (6 runs)

Instrumental constant	Value
X_P	0.966 ± 0.011
X_S	0.106 ± 0.005
X_δ	0.109 ± 0.006
ξ_P	1.120 ± 0.007
ξ_S	1.110 ± 0.007

Appendix B

Table B1: Description of the variables used in the approach.

Variable	Description
z	Height.
a	Atmospheric polarization parameter. Varies with height z.
δ	Atmospheric volume depolarization ratio, so that $\delta = \frac{1-a}{1+a}$.
δ_{mol}	Volume depolarization ratio in the free-aerosol region. Assumed constant and known.
β	Backscattering coefficient. Equal to the element F_{11} from the atmospheric scattering matrix.
β_{in}	Backscatter that arrives the receiver and it is measured by the total channel, $\beta_{in} = \beta$ in our system $(D_{tot} = 1)$
$\beta_{II,in}$	Parallel component of the arriving backscatter (with respect to the axis P).
$\beta_{\perp,in}$	Cross component of the arriving backscatter (with respect to the axis S).
T	Atmospheric transmission path for the lidar equation.
P_0	Number of emitted photons.
ε_l	Portion of the emitted radiation polarized in the cross direction ($\perp$), called crosstalk of the emitter.
I_L	Stokes vector describing the emitted radiation in terms of the polarization state.
F	Scattering matrix of the atmosphere. The element F_{11} corresponds to the backscattering coefficient β.
I_{in}	Stokes vector describing the arriving radiation after being transmitted, backscattered and depolarized by the atmosphere.
$c_{2\alpha}$	$\cos(2\alpha)$, α denotes the rotation between the polarization axis of the emission respect to the reception.
$R(\alpha)$	Rotation matrix to consider the effect of the rotation α between emission and receiver polarization plane.
$N_i(z)$	Number of photons measured by each detector (i=P, S, tot) at height z.
$\eta_{II,P}$	Constant describing the efficiency of the channel P to the component II.
$\eta_{\perp,S}$	Constant describing the efficiency of the channel S to the component $\perp$.
η_{tot}	Constant describing the efficiency of the total channel (tot) to the sum of the components $II+\perp$.
D_i	Efficiency ratio of each channel, $= \eta_{\perp,i}/\eta_{II,i}$ (i = P,S). $D_{tot} \equiv 1$ (ideal).
ε_r	So-called crosstalk of the receiver. $\varepsilon_r = D_P = D_S^{-1}$ (ideal case).
X_P	So-called interchannel constant, similar to the gain ratio used in previous studies (η^*). $\eta_{tot}/[\eta_{II,P}(1 + \varepsilon_r)]$

X_S	$\eta_{tot}/[\eta_{\perp,S}(1+\varepsilon_r)]$
X_δ	$\eta_{II,P}/\eta_{\perp,S} = X_S/X_P$
R_P	Ratio of signals $N_P(z)/N_{tot}(z)$
R_S	Ratio of signals $N_S(z)/N_{tot}(z)$
R_δ	Ratio of signals $N_S(z)/N_P(z)$
ξ_{tot}	So-called total crosstalk of the system (ideal case). It summarizes the 3 instrumental effects considered ($\varepsilon_l, c_{2\alpha}$ and ε_r).
ξ_P	Total crosstalk of the P channel (non-ideal case).
ξ_S	Total crosstalk of the S channels (non-ideal case).
ξ_S^P	$= (\xi_P^{-1} - \xi_S^{-1})/2$
$\Delta R_i(z_j, z_k)$	$= R_P(z_j) - R_S(z_k)$

Additional information about the extended 3-signal calibration approach.

- The extinction coefficient is assumed to be independent of the polarization state of the light. This assumption permits the simplification of the three lidar equations making possible the determination of the instrumental constants.

- The effects of the emission and reception in terms of polarization can be summarized into one total crosstalk constant ξ_{tot} (in the ideal case), or into two total crosstalk ξ_P and ξ_S for the non-ideal case (Appendix A).

- Differences with previous studies in terms of the nomenclature are present:
  - In our approach ε to denotes crosstalk, and not the error angle of the Δ90 calibration as denoted in previous studies. The crosstalk has been usually denoted by G_S and H_S (Freudentaler, 2016).
  - D_i denotes the efficiency ratio (Reichardt et al., 2003), while in recent studies D denotes the diattenuation parameter.

- The total channel is assumed to be ideal in terms of polarization, i.e. $D_{tot} = 1$.

- No diattenuation and retardation is considered in the emission and reception units.

References

Behrendt, A., and Nakamura, T.: Calculation of the calibration constant of polarization lidar and its dependency on atmospheric temperature, Opt. Express, 10, 805-817, 2002.

Belegante, L., Bravo-Aranda, J. A., Freudenthaler, V., Nicolae, D., Nemuc, A., Ene, D., Alados-Arboledas, L., Amodeo, A., Pappalardo, G., D'Amico, G., Amato, F., Engelmann, R., Baars, H., Wandinger, U., Papayannis, A., Kokkalis, P., and

Pereira, S. N.: Experimental techniques for the calibration of lidar depolarization channels in EARLINET, Atmos. Meas. Tech., 11, 1119-1141, https://doi.org/10.5194/amt-11-1119-2018, 2018.

Biele, J., Beyerle, G., and Baumgarten, G.: Polarization lidar: Corrections of instrumental effects, Opt. Express, 7,427-435, 2000.

Bissonnette, L. R., Bruscaglioni, P., Ismaelli, A., Zaccanti, G., Cohen, A., Benayahu, Y., Kleiman, M., Egert, S., Flesia, C., Schwendimann, P., Starkov, A. V., Noormohammadian, M., Oppel, U. G., Winker, D. M., Zege, E. P., Katsev, I. L., and Polonsky, I. N.: LIDAR multiple scattering from clouds, Appl. Phys. B, 60, 355-362, https://doi.org/10.1007/BF01082271, 1994.

Bravo-Aranda, J. A., Belegante, L., Freudenthaler, V., Alados-Arboledas, L., Nicolae, D., Granados-Muñoz, M. J., Guerrero-Rascado, J. L., Amodeo, A., D'Amico, G., Engelmann, R., Pappalardo, G., Kokkalis, P., Mamouri, R., Papayannis, A., Navas-Guzmán, F., Olmo, F. J., Wandinger, U., Amato, F., and Haeffelin, M.: Assessment of lidar depolarization uncertainty by means of a polarimetric lidar simulator, Atmos. Meas. Tech., 9, 4935-4953, https://doi.org/10.5194/amt-9-4935-2016, 2016.

Chen, W. N., Chiang, C. W., Nee, J. B.: Lidar ratio and depolarization ratio for cirrus clouds, Appl. Opt., 41, 6470-6476, https://doi.org/10.1364/AO.41.006470, 2002.

Chipman, R. A.: Mueller matrices in: Handbook of Optics, Volume I, 3rd Edn., chap. 14, McGraw-Hill, 2009.

David, G., Miffre, A., Thomas, B., and Rairoux, P.: Sensitive and accurate dual-wavelength UV-VIS polarization detector for optical remote sensing of tropospheric aerosols, Appl. Phys. B, 108, 197–216, https://doi.org/10.1007/s00340-012-5066-x, 2012.

Donovan, D. P., Klein Baltink, H., Henzing, J. S., de Roode, S. R., and Siebesma, A. P.: A depolarisation lidar-based method for the determination of liquid-cloud microphysical properties, Atmos. Meas. Tech., 8, 237-266, https://doi.org/10.5194/amt-8-237-2015, 2015.

Eloranta, E. W.: Practical model for the calculations of multiply scattered lidar returns, Appl. Optics, 37, 2464-2472, 1998.

Engelmann, R., Kanitz, T., Baars, H., Heese, B., Althausen, D., Skupin, A., Wandinger, U., Komppula, M., Stachlewska, I. S., Amiridis, V., Marinou, E., Mattis, I., Linné, H., and Ansmann, A.: The automated multiwavelength Raman polarization and water-vapor lidar PollyXT: the neXT generation, Atmos. Meas. Tech., 9, 1767–1784, https://doi.org/10.5194/amt-9-1767-2016, 2016.

Fan J., Wang Y., Rosenfeld D., and Liu X.: Review of Aerosol-Cloud Interactions: Mechanisms, significance, and Challenges, J. Atmospheric Sci., 73, 4221-4252, https://doi.org/10.1175/JAS-D-16-0037.1, 2016.

Freudenthaler, V., Esselborn, M., Wiegner, M., Heese, B., Tesche, M., Ansmann, A., Müller, D., Althausen, D., Wirth, M., Fix, A., Ehret, G., Knippertz, P., Toledano, C., Gasteiger, J., Garhammer, M., and Seefeldner, M.: Depolarization ratio profiling at several wavelengths in pure Saharan dust during SAMUM 2006, Tellus B, 61, 165–179, https://doi.org/10.1111/j.1600- 0889.2008.00396.x, 2009.

Freudenthaler, V.: About the effects of polarising optics on lidar signals and the Δ90 calibration, Atmos. Meas. Tech., 9, 4181-4255, https://doi.org/10.5194/amt-9-4181-2016, 2016.

5   Freudenthaler, V., Seefeldner, M., Groß, S., and Wandinger., U.: Accuracy of Linear Depolarisation Ratios in Clean Air Ranges Measured with POLIS-6 at 355 and 532 NM, EPJ Web of Conferences 119, 25013, https://doi.org/10.1051/epjconf/201611925013, 2016b.

Groß, S., Freudenthaler, V., Schepanski, K., Toledano, C., Schäfler, A., Ansmann, A., and Weinzierl, B.: Optical
10   properties of long-range transported Saharan dust over Barbados as measured by dual-wavelength depolarization Raman lidar measurements, Atmos. Chem. Phys., 15, 11067-11080, https://doi.org/10.5194/acp-15-11067-2015, 2015.

Haarig, M., Ansmann, A., Althausen, D., Klepel, A., Groß, S., Freudenthaler, V., Toledano, C., Mamouri, R.-E., Farrell, D. A., Prescod, D. A., Marinou, E., Burton, S. P., Gasteiger, J., Engelmann, R., and Baars, H.: Triple-wavelength
15   depolarization-ratio profiling of Saharan dust over Barbados during SALTRACE in 2013 and 2014, Atmos. Chem. Phys., 17, 10767-10794, https://doi.org/10.5194/acp-17-10767-2017, 2017.

Haarig, M., Ansmann, A., Baars, H., Jimenez, C., Veselovskii, I., Engelmann, R., and Althausen, D.: Depolarization and lidar ratios at 355, 532, and 1064 nm and microphysical properties of aged tropospheric and stratospheric Canadian
20   wildfire smoke, Atmos. Chem. Phys., 18, 11847-11861, https://doi.org/10.5194/acp-18-11847-2018, 2018.

Hogan, R. J.: Fast Lidar and Radar Multiple-Scattering Models. Part I: Small-Angle Scattering Using the Photon Variance-Covariance Method, J. Atm. Sci., 65, 3621-3635, 2008.

25   Hogan, R. J., Haywood, J. M., Westbrook, C. D., Dacre, H. F., Marenco, F., O'Connor, E. J., Johnson, B. T., Wrench, C. L., and Belcher, S. E.: Combined lidar and sun photometer retrievals of ash particle size and mass concentration from the Eyjafjallajökull volcano, J. Geophys. Res., in press, 2012.

Hu, Y., Vaughan, M., Liu, Z., Lin, B., Yang, P., Flittner, D., Hunt, B., Kuehn, R., Huang, J., Wu, D., Rodier, S., Powell,
30   K., Trepte, C., and Winker, D.: The depolarization − attenuated backscatter relation: CALIPSO lidar measurements vs. theory, Opt. Express 15, 5327–5332, 2007.

Huang, Y., Chameides, W. L., and Dickinson, R. E.: Direct and indirect effects of anthropogenic aerosols on regional precipitation over east Asia, J. Geophys. Res., 112, D03212, doi:10.1029/2006JD007114, 2007.

35

IPCC: Climate Change 2014: Synthesis Report. Contribution of Working Groups I, II and III to the Fifth Assessment Report of the Intergovernmental Panel on Climate Change, edited by: Core Writing Team, Pachauri, R.K., and Meyer, L.A., IPCC, Geneva, Switzerland, 151 pp; available at: https://www.ipcc.ch/pdf/assessment-report/ar5/syr/SYR_AR5_FINAL_full.pdf, 2014.
40

Jimenez, C., Ansmann, A., Donovan, D., Engelmann, R., Malinka, A., Schmidt, J., and Wandinger, U.: Retrieval of microphysical properties of liquid water clouds from atmospheric lidar measurements: Comparison of the Raman dual field of view and the depolarization techniques, Proc. SPIE 10429, 1042907, https://doi.org/10.1117/12.2281806, 2017.

Jimenez, C., Ansmann, A., Donovan, D., Engelmann, R., Schmidt, J., and Wandinger, U.: Comparison between two lidar methods to retrieve microphysical properties of liquid water clouds, EPJ Web Conf., 176, 01032, https://doi.org/10.1051/epjconf/201817601032, 2018.

5 Jimenez, C., Ansmann, A., Engelmann, R., Malinka, A., Schmidt, J., and Wandinger, U.: Retrieval of microphysical properties of liquid water clouds from atmospheric lidar measurements: dual field of view depolarization technique, Atmos. Meas. Tech. (working paper), 2018b.

Kanitz, T., Seifert, P., Ansmann, A., Engelmann, R., Althausen, Casiccia, C., and Rohwer, E. G.: Contrasting the impact
10 of aerosols at northern and southern midlatitudes on heterogeneous ice formation, Geophys. Res. Lett., 38, L17802, doi:10.1029/2011GL048532, 2011.

Li, J., Jian, B., Huang, J., Hu, Y., and Wu, M.: Long-term variation of cloud droplet number concentrations from space-based Lidar, Rem. Sens. Environment, 213, 144-161, 2018

Liu, B., and Wang, Z.: Improved calibration method for depolarization lidar measurement, Opt. Express, 21, 14583-14590, https://doi.org/10.1364/OE.21.014583, 2013.

Lu, S. Y., and Chipman, R. A.: Interpretation of Mueller matrices based on polar decomposition, J. Opt. Soc. Am. A, 13,
20 1106–1113, 1996.

Malinka, A.V, and Zege, E.P.: Analytical modeling of Raman lidar return, including multiple scattering, Appl. Optics, 42, 1075-1081, 2003.

25 Malinka, A. V., and Zege, E. P.: Possibilities of warm cloud microstructure profiling with multiple-field-of-view Raman lidar, Appl. Optics 46, 8419–8427, 2007.

Mamouri, R. E., and Ansmann, A.: Potential of polarization lidar to provide profiles of CCN- and INP-relevant aerosol parameters, Atmos. Chem. Phys., 16, 5905-5931, https://doi.org/10.5194/acp-16-5905-2016, 2016.
30

Mattis, I., Ansmann, A., Müller, D., Wandinger, U., and Althausen, D.: Multiyear aerosol observations with dualwavelength Raman lidar in the framework of EARLINET, J. Geophys. Res., 109, D13203, doi:10.1029/2004JD004600, 2004.

35 Mattis, I., Müller, D., Ansmann, A., Wandinger, U., Preißler, J., Seifert, P., and Tesche, M.: Ten years of multiwavelength Raman lidar observations of free-tropospheric aerosol layers over central Europe: Geometrical properties and annual cycle, J. Geophys. Res., 113, D20202, doi:10.1029/2007JD009636, 2008.

Mattis, I., Tesche, M., Grein, M., Freudenthaler, V., and Müller, D.: Systematic error of lidar profiles caused by a
40 polarization-dependent receiver transmission: quantification and error correction scheme, Appl. Optics, 48, 2742-2751, 2009.

Mattis, I., Seifert, P., Müller, D., M. Tesche, Hiebsch, A., Kanitz, T., Schmidt, J., Finger, F., Wandinger, U., and Ansmann, A.: Volcanic aerosol layers observed with multiwavelength Raman lidar over central Europe in 2008–2009, J. Geophys. Res., 115, D00L04, doi:10.1029/2009JD013472, 2010.

5   McCullough, E. M., Sica, R. J., Drummond, J. R., Nott, G., Perro, C., Thackray, C. P., Hopper, J., Doyle, J., Duck, T. J., and Walker, K. A.: Depolarization calibration and measurements using the CANDAC Rayleigh–Mie–Raman lidar at Eureka, Canada, Atmos. Meas. Tech., 10, 4253-4277, https://doi.org/10.5194/amt-10-4253-2017, 2017.

McCullough, E. M., Sica, R. J., Drummond, J. R., Nott, G. J., Perro, C., and Duck, T. J.: Three-channel single-wavelength
10 lidar depolarization calibration, Atmos. Meas. Tech., 11, 861-879, https://doi.org/10.5194/amt-11-861-2018, 2018.

Okamoto, H., Sato, K., Makino, T., Nishizawa, T., Sugimoto, N., Jin, Y., and Shimuzi, A.: Depolarization ratio of clouds measured by multiple –field of view multiple scattering polarization lidar, EPJ Web Conf., 119, 11007, ILRC 27, https://doi.org/10.1051/epjconf/201611911007, 2016.

Pappalardo, G., Amodeo, A., Apituley, A., Comeron, A., Freudenthaler, V., Linne, H., Ansmann, A., Bösenberg, J., D'Amico, G., Mattis, I., Mona, L., Wandinger, U., Amiridis, V., Alados-Arboledas, L., Nicolae, D., and Wiegner, M.: EARLINET: towards an advanced sustainable European aerosol lidar network, Atmos. Meas. Tech., 7, 2389-2409, doi:10.5194/amt-7-2389-2014, 2014.

Reichardt, J., Baumgart, R., and McGee, T. J.: Three-signal method for accurate measurements of depolarization ratio with lidar, Appl. Opt, 42, 4909-4913, 2003.

Schmidt, J., Wandinger, U., and Malinka, A.: Dual-field-of-view Raman lidar measurements for the retrieval of cloud
25 microphysical properties, Appl. Optics 52, 2235–2247, 2013.

Schmidt, J., Ansmann, A., Bühl, J., Baars, H., Wandinger, U., Müller, D., and Malinka, A. V.: Dual-FOV Raman and Doppler lidar studies of aerosol-cloud interactions: Simultaneous profiling of aerosols, warm-cloud properties, and vertical wind, J. Geophys. Res. Atmos., 119, 5512–5527, 2013b.

30

Schmidt, J., Ansmann, A., Bühl, J., and Wandinger, U.: Strong aerosol–cloud interaction in altocumulus during updraft periods: lidar observations over central Europe, Atmos. Chem. Phys., 15, 10687-10700, https://doi.org/10.5194/acp-15-10687-2015, 2015.

35 Sekiguchi, M., Nakajima, T., Suzuki, K., Kawamoto, K., Higurashi, A., Rosenfeld, D., Sano, I., and Mukai, S.: A study of the direct and indirect effects of aerosols using global satellite data sets of aerosol and cloud parameters, J. Geophys. Res., 108(D22), 4699, doi:10.1029/2002JD003359, 2003.

Stelmaszczyk, K., Dell'Aglio, M., Chudziński, S., Stacewicz, T., and Wöste, L.: Analytical function for lidar geometrical
40 compression form-factor calculations, Appl. Opt., 44, 1323-1331, 2005.

Twomey, S.: Influence of pollution on shortwave albedo of clouds, J. Atmos. Sci., 34, 1149–1152, 1977.